Coronal Magnetic Field Extrapolation and Topological Analysis of Fine-scale Structures during Solar Flare Precursors

Wen He[1] , Ju Jing[2] , Haimin Wang[2] , Sushree S. Nayak[3] , and Avijeet Prasad[4,5]
[1] Department of Space Science, The University of Alabama in Huntsville, Huntsville, AL 35805, USA; wh0032@uah.edu
[2] Center for Solar-Terrestrial Research, New Jersey Institute of Technology, University Heights, Newark, NJ 07102-1982, USA
[3] Center for Space Plasma and Aeronomic Research (CSPAR), The University of Alabama in Huntsville, Huntsville, AL 35805, USA
[4] Institute of Theoretical Astrophysics, University of Oslo, Postboks 1029 Blindern, NO-0315 Oslo, Norway
[5] Rosseland Centre for Solar Physics, University of Oslo, Postboks 1029 Blindern, NO-0315 Oslo, Norway

Abstract

Magnetic field plays an important role in various solar eruption phenomena. The formation and evolution of the characteristic magnetic field topology in solar eruptions are critical problems that will ultimately help us understand the origin of these eruptions in the solar source regions. With the development of advanced techniques and instruments, observations with higher resolutions in different wavelengths and fields of view have provided more quantitative information for finer structures. It is therefore essential to improve the method with which we study the magnetic field topology in the solar source regions by taking advantage of high-resolution observations. In this study, we employ a nonlinear force-free field extrapolation method based on a nonuniform grid setting for an M-class flare eruption event (SOL2015-06-22T17:39) with embedded vector magnetograms from the Solar Dynamics Observatory (SDO) and the Goode Solar Telescope (GST). The extrapolation results for which the nonuniform embedded magnetogram for the bottom boundary was employed are obtained by maintaining the native resolutions of the corresponding GST and SDO magnetograms. We compare the field line connectivity with the simultaneous GST/Hα and SDO/Atmospheric Imaging Assembly observations for these fine-scale structures, which are associated with precursor brightenings. Then we perform a topological analysis of the field line connectivity corresponding to fine-scale magnetic field structures based on the extrapolation results. The analysis results indicate that when we combine the high-resolution GST magnetogram with a larger magnetogram from the SDO, the derived magnetic field topology is consistent with a scenario of magnetic reconnection among sheared field lines across the main polarity inversion line during solar flare precursors.

Unified Astronomy Thesaurus concepts: Solar flares (1496); Solar active region magnetic fields (1975); Solar magnetic fields (1503)

1. Introduction

Different types of spectacular eruptions in the solar atmosphere such as flares, coronal mass ejections (CMEs), and jets release energy on various spatial and temporal scales. In particular, a solar flare eruption attracts much attention among these eruption phenomena as an explosive, energetic phenomenon with enhanced emission throughout the electromagnetic spectrum in a dynamic and complicated process. In multiwavelength observations, a flare usually goes through three major phases: the preflare, the impulsive, and the gradual phase. The life of a flare spans from tens of seconds to several hours (see the review by Benz 2017). During the flare eruption, the energy release can be as large as 10^{32} erg, while the main contribution comes from the magnetic energy compared to other sources. To determine the underlying physical mechanisms, i.e., the source of the energy that is released, much effort has been made from the different perspectives to study the main phase (impulsive and gradual phase) of solar flares. For example, the standard two-dimensional flare model (so-called CSHKP model; Carmichael 1964; Sturrock 1966; Hirayama 1974; Kopp & Pneuman 1976) proposes that magnetic

reconnection plays the main role in the energy release during the evolution of a flare.

In addition to the main phase of the flare eruption, it is noteworthy that there are also some interesting small-scale localized energy-release phenomena in the precursor phase (before the main phase of the flare or before the time of the peak X-ray flux emission), e.g., the so-called flare precursor brightenings. Bumba & Křivský (1959) introduced the concept of flare precursors, which were observed as a short-term and small brightening before the onset of the main flare. It was later observed in many flares through multiple wavelengths, including X-ray, optical, ultraviolet/extreme ultraviolet (UV/EUV), and microwave observations (Awasthi et al. 2014; Bamba et al. 2014, 2017). Tappin (1991) performed a statistical study based on X-ray observations to investigate the correlation between flare precursors and flare onsets, and they summarized that most flares as measured by X-ray emissions are preceded by one or more soft X-ray precursors with 10–60 minutes prior to the flare onset (see also the more recent statistical study by Gyenge et al. 2016). Later, Chifor et al. (2007) reported that the precursors that are located near or on the polarity-inversion line (PIL) and hard X-ray precursor brightenings rapidly move along the PIL before the main phase of the flare. This was based on the analysis of a list of preflare events for which multiwavelength observations were combined with the evolution of photospheric magnetic fields. The study of Chifor and collaborators also provided evidence of the spatial and

temporal correlation between the preflare activities and the onset of the filament eruption. Therefore, the investigation of the flare precursors is an important subject not only for the initiation mechanism of flares, but also for the associated eruption phenomena. Because the energy release of the flare precursors is smaller than that of the main phase of the flare evolution, observations at higher spatial and temporal resolutions are required. On the other hand, it is also essential to validate different eruption initiation mechanisms with a better understanding of the magnetic field topology for flare precursors. However, the inherent fine-scale three-dimensional (3D) magnetic field topology change is still unclear because we lack a quantitative study that uses high-resolution vector magnetograms. Here we intend to perform an analysis of the fine-scale magnetic field structures associated with flare precursor brightenings through extrapolations of the nonlinear force-free field (NLFFF) by employing high-resolution vector magnetograms from multiple sources that have recently become available.

With the recent development of observational techniques and instruments, more advanced high-resolution solar observational data become available, including those from space-based telescopes such as the Solar Dynamics Observatory (SDO), the Hinode satellite, and Solar Orbiter, and also from ground-based telescopes such as the 1.6 m Goode Solar Telescope (GST), the 4 m Daniel K. Inouye Solar Telescope (DKIST), and so on. More advanced observations will be definitely crucial to improve our understanding of small-scale energy-release processes such as flare precursors and their connections to the following main phase of the flare. Therefore, there is a growing demand for taking full advantage of data from multiple instruments with the necessary improvements of existing methods. For instance, an ultrahigh-resolution observation in a smaller field of view (FOV) can contribute to the analysis of the fine-scale structure of small-scale events (Jing et al. 2016; Wang et al. 2017; Zhao et al. 2022). Alternatively, a relatively lower-resolution observation in a larger FOV can better extend the spatial coverage and describe the magnetic connections to surrounding structures. For the analysis of coronal magnetic structures in solar eruptions, vector magnetograms may be obtained from multiple instruments with different spatio-temporal resolutions and FOVs (mostly on the photosphere). One desirable approach is to be able to combine these vector magnetograms for the numerical extrapolation of the coronal magnetic field while preserving their respective advantages.

Numerical simulations can be a viable tool for deriving unavailable data such as the 3D coronal magnetic fields with reasonable assumptions (Jiang et al. 2022). For example, photospheric vector magnetograms are often employed as bottom boundary conditions (BCs) in different numerical simulation methods to reconstruct the 3D coronal magnetic field in the solar source region. However, the limitations of computational resources for the numerical simulation capability of a more realistic full magnetohydrodynamics (MHD) model also lead to the use of the NLFFF extrapolation method to reconstruct static 3D coronal magnetic field based on a force-free assumption (Jiang & Feng 2012; Wiegelmann & Sakurai 2021). Different types of numerical methods have been proposed to reconstruct the NLFFF for the coronal magnetic field from specific BCs and sometimes also pseudo-initial conditions, including the upward integration, Grad–Rubin iteration, MHD relaxation, optimization approach (see the review by Wiegelmann & Sakurai 2021). The computation

speed and quality of different numerical modeling results may vary significantly for the realistic solar magnetograms, not only due to the differences in algorithms and their specific realizations, but also due to the quality of the input magnetograms. For instance, the spatial resolution of input vector magnetograms, because the bottom BC has been proven to have an essential effect on NLFFF extrapolation results, including the magnetic energy and associated magnetic field topology, as reported by Thalmann et al. (2013) and DeRosa et al. (2015). On the other hand, more solar observations become available and can provide vector magnetograms in different spatial resolutions and FOVs for the same solar source region. Therefore, in order to improve the computational efficiency and maximize the advantage of available observations, it becomes natural to incorporate the available higher-resolution magnetograms (often in a small FOV) in the bottom BC along with the lower-resolution magnetograms (with a larger FOV) to conduct the extrapolation, thus maintaining the native resolution of the higher-resolution magnetogram and a larger FOV at the same time, especially for the study of fine-scale structure in flare precursors.

An M6.5 class flare erupted close to the solar disk center (8° W 12°N) on 2015 June 22 in active region NOAA 12371. The impulsive phase of the flare starts at ~17:51 UT. Two short-duration small-scale brightenings were observed in unprecedented spatio-temporal resolution by the 1.6 m GST, along with photospheric magnetic field dynamics, and they were reported as flare precursors by Wang et al. (2017). These authors focused on two short episodes of the flare precursors by using high-resolution Hα observations and observations of the photospheric magnetic field from the GST, complemented by X-ray and microwave observations. These observations indicated a successive reconnection process during the evolution of the precursor periods that may contribute to the onset of the main flare. Many studies have been performed for this event in terms of different physical processes. The fine-scale structure of this flare and the associated large-scale dynamical motion of flare ribbons have been discussed by Jing et al. (2016, 2017). Liu et al. (2018) and Xu et al. (2018) studied the relation between the flaring signatures and the evolution of photospheric vector magnetic fields by taking advantage of the GST observations. For the flare onset process, some authors (Awasthi et al. 2018; Kang et al. 2019; Liu et al. 2022b) have studied the pre-eruptive magnetic configuration with a reconstructed 3D magnetic field by the NLFFF extrapolation method, which is based on magnetograms obtained with the SDO/Helioseismic and Magnetic Imager (HMI; Schou et al. 2012). A multi-instrument comparative study was also conducted by Liu et al. (2022a). This study offers a quantitative description of the thermal behaviors for a flare precursor over a large temperature range. In addition, Jing et al. (2023) analyzed the 3D magnetic properties of two light bridges in both small and large scales before the flare by using the photospheric vector magnetograms from GST and SDO separately for the NLFFF extrapolation. For all these studies, it is always essential to compare the derived magnetic field configuration with the corresponding multiwavelength imaging observations to help validate and interpret the extrapolation results when applicable.

In this study, we apply a type of MHD relaxation method with a conservation-element/solution-element (CESE) solver, the so-called CESE-MHD-NLFFF method (see details in Jiang et al.

2011; Jiang & Feng 2013) to obtain the 3D coronal magnetic field in an approximately force-free state. This has been widely applied to the analysis of magnetic field topology with realistic solar magnetic field data (Jiang & Feng 2013; Duan et al. 2017, 2019; He et al. 2022). For example, in our previous study, this method was applied to characterize the properties of magnetic flux ropes (MFRs) on the Sun, and the results were then quantitatively compared to the properties of the corresponding interplanetary counterparts (He et al. 2022). The results indicated the importance of the flare-associated magnetic reconnection process in that the magnetic reconnection flux estimated from the analysis corresponds well to the magnetic flux content found in the MFR that formed during the main phase of solar flares. A subsequent study (Hu et al. 2022) further implied the variability in the magnetic field topology changes of an MFR as manifested in the analysis of multiple observations of the associated flare/CME eruption process. For the present study, with the available high-resolution GST observations for the aforementioned M6.5 flare, we develop a modified version of the existing CESE-MHD-NLFFF code for embedded magnetograms by incorporating the high-resolution GST magnetogram and the larger FOV SDO/HMI magnetogram as the bottom BC with a nonuniform grid spacing. The results are compared to the extrapolations with single-set uniform magnetograms and the associated observations, mainly the high-resolution GST/Hα images during the flare precursors.

The article is organized as follows. First, the instrumentation and data used in this paper are described in Section 2. Then we present the modified CESE-MHD-NLFFF method and the associated convergence study in Section 3. In Section 4, the magnetic field topology from the extrapolations with different bottom BCs is presented and investigated in detail. The main results are summarized and the conclusions are given in Section 5.

2. Instrumentation and Data

For this event, we make use of the observational data from both SDO and GST. SDO routinely provides full-disk observations of the Sun. Specifically, the Space-weather HMI Active Region Patch (SHARP; Bobra et al. 2014) vector magnetograms are used as the input bottom BCs of the NLFFF extrapolations. The SHARP data product offers photospheric vector magnetograms with a pixel size of $0\rlap{.}''5$ ($\sim$365 km) in a cadence of 720 s. On the other hand, the corresponding remote-sensing observations in UV and EUV wavelength channels are provided by the Atmospheric Imaging Assembly (AIA; Lemen et al. 2012) on board SDO with a spatial sampling of around $0\rlap{.}''6$ pixel^{-1} ($\sim$438 km) and a moderate time cadence (12 s for EUV channels, and 24 s for UV channels). For the 2015 June 22 flare event, the GST at the Big Bear Solar Observatory (BBSO) also obtained high-resolution observations during $\sim$16:50–23:00 UT (Jing et al. 2016; Wang et al. 2017). The Hα images at the line center and off-bands ($\pm$0.6 Å and $\pm$1.0 Å) are taken by the Visible Imaging Spectrometer (VIS; Cao et al. 2010) with a FOV of $\sim 57'' \times 64''$ (42×47 Mm^2). The GST/VIS observations have a pixel size as small as $\sim 0\rlap{.}''03$ ($\sim$22 km) and a time cadence of 28 s. The Near InfraRed Imaging Spectropolarimeter (NIRIS; Cao et al. 2012) of the GST, equipped with the infrared detector and a dual Fabry–Perot interferometers system, provides the spectropolarimetric data (at the Fe I 1565 nm doublet, 0.2 Å bandpass). The spectropolarimetric data are processed with the NIRIS data-

processing pipeline, including dark and flat field corrections, instrument crosstalk calibration, and Milne–Eddington Stokes inversion, from which the vector magnetic fields can be extracted. The pixel size and temporal cadence of the resulting vector magnetograms are $\sim 0\rlap{.}''08$ ($\sim$59 km) and 87 s. For this event, the GST/NIRIS vector magnetograms and the SDO/HMI products have been properly aligned and compared at about the same time by Liu et al. (2018), and both the horizontal and vertical magnetic fields from NIRIS and HMI measurements show a high correlation (with correlation coefficients greater than 0.85) for the core region of the flare.

In general, the space-borne instrumentation provides a larger FOV and more continuous observations, while the ground-based counterpart has a relatively smaller FOV and more sporadic temporal coverage, but its spatial resolution is much higher. Therefore, it is desirable to combine these two sets of observations in order to make the best use of their data products by embedding the higher-resolution GST/NIRIS magnetogram into the corresponding part of the lower-resolution SDO/HMI magnetogram with the larger FOV.

To generate such a comprehensive NIRIS-HMI magnetogram, the first and most important step is the time-consuming alignment of the NIRIS and HMI magnetograms. Using the data here as an example, the FOV of the NIRIS magnetogram is $52'' \times 52''$ (38×38 Mm^2), consisting of 650×650 pixels with a spatial sampling of $0\rlap{.}''08$ pixel^{-1}, while the FOV of HMI is about $200'' \times 200''$ (146×146 Mm^2), consisting of 400×400 pixels, $0\rlap{.}''5$ pixel^{-1}. By manual alignment, we find the exact position, with subpixel precision, of the NIRIS magnetogram of a small FOV on the HMI magnetogram of a large FOV. Because the spatial sampling rates of the two magnetograms are different, we interpolate the data array of the HMI magnetogram to 2500×2500 pixels with the same FOV, so that each of its pixels has the same spatial scale as the NIRIS magnetogram, i.e., $0\rlap{.}''08$ pixel^{-1}. Then, we embed the GST/NIRIS magnetogram in the middle of this HMI magnetogram. After these steps, an embedded magnetogram with a FOV of $200'' \times 200''$ (146×146 Mm^2) and a pixel size of $0\rlap{.}''08$ pixel^{-1} ($\sim$60 km pixel^{-1}) is derived that contains data from both HMI and NIRIS. However, it is very costly to perform computations for such a magnetogram with a uniform ultrahigh resolution. We constructed a nonuniform grid structure for the NLFFF extrapolations and used the embedded magnetograms with nonuniform resolutions as our bottom BC.

3. NLFFF Extrapolation Code for Embedded Magnetograms

3.1. Extrapolation Method by the CESE-MHD-NLFFF Code

The CESE-MHD-NLFFF code is similar to a magnetofrictional method, which can be regarded as a special case of the MHD relaxation method. It is mainly designed to solve the modified momentum equation and the magnetic induction equation (Jiang & Feng 2012, 2013),

$$\frac{\partial(\rho \boldsymbol{v})}{\partial t} = (\nabla \times \boldsymbol{B}) \times \boldsymbol{B} - \nu \rho \boldsymbol{v}, \quad \rho = |\boldsymbol{B}|^2 + \rho_0, \quad (1)$$

$$\frac{\partial \boldsymbol{B}}{\partial t} = \nabla \times (\boldsymbol{v} \times \boldsymbol{B}) - \boldsymbol{v} \nabla \cdot \boldsymbol{B} + \nabla(\mu \nabla \cdot \boldsymbol{B}). \quad (2)$$

These equations are solved as a kind of Dirichlet-type boundary value problem. Based on the force-free field assumption (plasma $\beta \ll 1$), the magnetic force plays a major

role. Other forces, including the plasma pressure, gravity, and inertial forces, can therefore be ignored. In order to balance the Lorentz force, an artificial term $\nu\rho v$ in a frictional force form involving velocity v is added to the momentum Equation (1). In addition, a pseudo-mass density ρ is assumed to take the form given. ρ is modified with a small value ρ_0, e.g., $\rho_0 = 0.1$ (in the same unit as $|B|^2$), to deal with the case of very weak magnetic field. For the magnetic induction equation, two additional terms are added to control the divergence of the magnetic field. Equations (1) and (2) are solved through the iteration process until a converged solution of a quasi-static equilibrium state is approached.

The computation proceeds by iterations until a converged solution is reached, as judged by a series of metrics. For the NLFFF extrapolation, a well-known problem is that the force-free condition may not always be satisfied in the inhomogeneous solar atmosphere, especially in the photosphere (Gary 2001). Wiegelmann et al. (2006) proposed that a more consistent bottom BC for an NLFFF extrapolation can be obtained by modifying the original photospheric magnetogram to mimic a force-free chromospheric magnetogram. The practice that is commonly adopted for NLFFF extrapolations is called preprocessing. The basic method for preprocessing proposed by Wiegelmann et al. (2006) is to obtain a target magnetogram by minimizing a function that includes several additional constraints through an optimization method. The individual constraints include the surface integrals of the total force, the total torque, the deviation of the updated magnetogram from the observed magnetogram, and the smoothness of the updated magnetogram. The optimization and smoothing algorithms can vary in different preprocessing codes. Here, we follow the basic approach of Wiegelmann et al. (2006), but use the specific preprocessing code developed by Jiang & Feng (2014) to determine the bottom BC for the CESE-MHD-NLFFF extrapolation code before the computation. This preprocessing code works by splitting the magnetogram into the potential field part and the nonpotential field part. Then the nonpotential part is optimized and smoothed following the general approach of Wiegelmann et al. (2006) to approach a force-free state. The preprocessed magnetogram can usually achieve the same level of force-freeness as the potential field part, as evaluated by the standard set of metrics (Jiang & Feng 2014).

3.2. Grid Construction and Modified CESE-MHD-NLFFF Code for Embedded Magnetograms

Considering the speed and accuracy of the computation for the realistic solar magnetograms, a nonuniform grid structure within a block-structured (one block contains a group of cells) parallel computation framework has been adopted for the CESE-MHD-NLFFF code with the help of the PARAMESH software package (MacNeice et al. 2000). For the grid initialization of the CESE-MHD-NLFFF code, the whole computational domain includes the preset central core region and the surrounding buffer region to reduce the influence of the side boundaries (Jiang & Feng 2013). Then the whole computational domain is divided into blocks with different spatial resolutions, and all blocks have identical logical structures. The blocks are evenly distributed among the processors. The block structures can be refined or de-refined,

which provides flexibility for embedding nonuniform magnetograms as bottom BCs.

To apply the embedded magnetograms with a nonuniform spatial resolutions for the NLFFF extrapolation, we develop a modified version of the CESE-MHD-NLFFF code to use the embedded map as the bottom BC. Figures 1(a) and (b) show the difference of the bottom boundary layers between the nonuniform embedded and uniform magnetograms. Specifically, we redesign the grid structure for the whole computational domain and embed the higher-resolution magnetogram within a rectangular region into the bottom boundary, forming the core region. An enlarged version of the bottom boundary surrounding the core region is presented in Figure 1(c). First, the initial grid structure should be built according to the uneven spatial resolutions of the embedded magnetogram before the computation. In PARAMESH, there is a routine to check the difference in the refinement level between the refined block and its neighboring blocks, which should be no more than one level. For example, in a uniform grid structure with grid size $dx = 8$, the grid size in the core region cannot be refined once to $dx = 1$ instantly, but it can only be refined once to $dx = 4$. To reach the finest grid size $dx = 1$, two additional intermediate regions are required with grid sizes $dx = 2$ and $dx = 4$ (see the illustration of the intermediate regions in Figure 1(d)). Therefore, for a nonuniform embedded magnetogram (the resolution ratio should be integral powers of two), we need additional intermediate regions between the central core region and the buffer region due to the constraint from the PARAMESH package. Different from the grid structure in a uniform magnetogram, which mainly consists of a core region and the surrounding buffer region, the bottom boundary for an embedded magnetogram is therefore mainly divided into three parts: the inner core region for the higher-resolution magnetogram (in a smaller FOV), the intermediate regions from the rebinned higher-resolution magnetogram, and the surrounding buffer region populated by the lower-resolution magnetogram (with a larger FOV). One important principle for our embedding is to keep the higher-resolution magnetogram in its entirety as much as possible, so that the intermediate regions between the core region and the buffer region are generally kept as narrow as possible. After the relative positions for the two aligned magnetograms are obtained, the grid structure for the whole computational domain can be set up.

After the grid initialization, the initial solutions for all blocks in the whole computation domain will be assigned by a potential field solution derived from the higher-resolution magnetogram in the core region via Green's function method (Chiu & Hilton 1977). On the bottom boundary, values from the higher-resolution magnetogram will be assigned to the innermost core region and the intermediate regions with proper rebinning. In contrast, the buffer region will adopt values from the lower-resolution magnetogram. The bottom BC is usually applied gradually, reaching the assigned values during the initial iteration steps, and then it will be fixed during the remainder of the computation.

3.3. Convergence Study and NLFFF Quality Metrics

To verify the quality and accuracy of the NLFFF extrapolation results, a routine check and evaluation of the extrapolated coronal magnetic field in a volume, including the force-freeness and divergence-freeness metrics, and a comparison with coronal observations are usually required, according to various
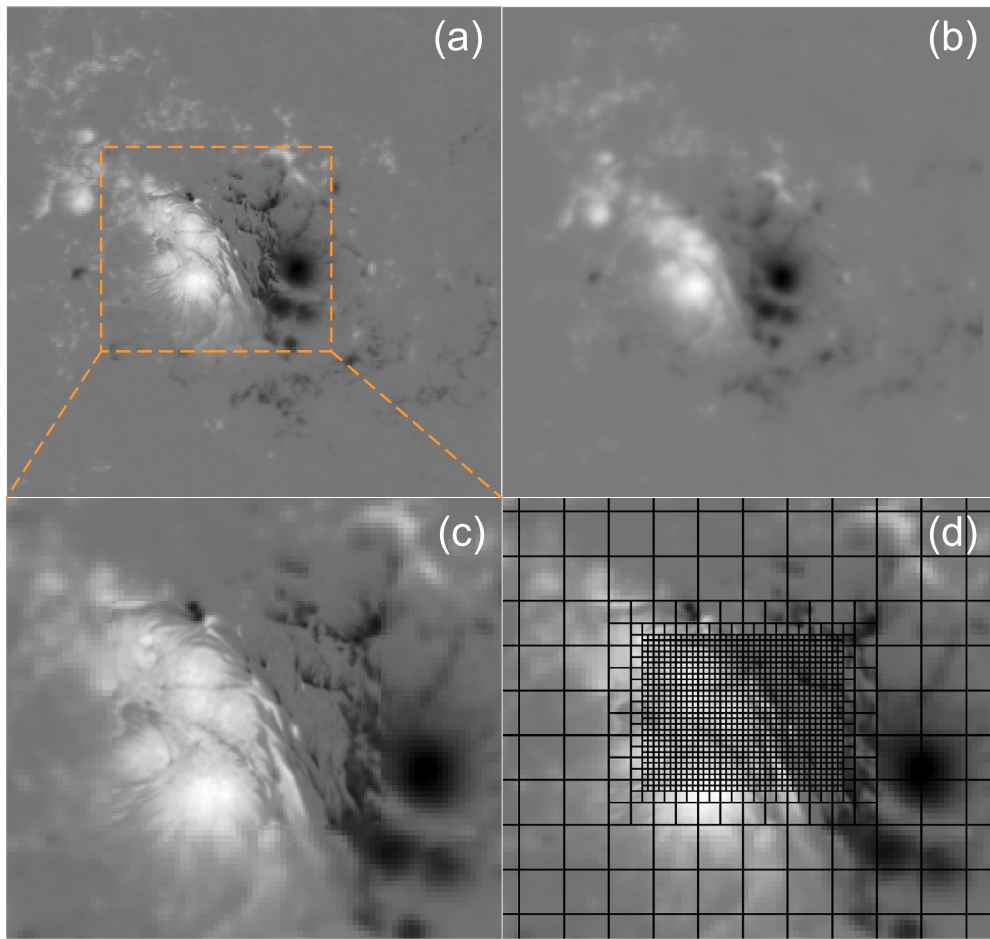
Figure 1. Bottom boundary layers of the B_z component for (a) the embedded magnetogram, (b) the uniform HMI magnetogram, and (c) a zoomed-in portion of (a) as outlined by the orange box. Panel (d) shows one associated nonuniform grid structure on the bottom boundary for (c). The whole domain is divided into blocks with equal sides, as illustrated in (d) for the bottom boundary by the solid lines, and each block contains $8 \times 8 \times 8$ cells. The side length of the cell for the innermost block is $0\rlap{.}''125$ (91 km), corresponding to the side length $1''$ (730 km) of the blocks that form the core region, as shown. It doubles three times to reach the cell size $1''$ for the outermost region, which is the buffer region. The intermediate region lies between these regions.

validation studies of NLFFF modeling results (Schrijver et al. 2006; Metcalf et al. 2008; DeRosa et al. 2015). In this study, we calculate several NLFFF quality metrics to examine the trend of the extrapolation results during the convergence process. The quality metrics include the residual of the field between two successive iteration steps; the *CWsin*, a current-weighted sine metric defined by the mean sine of the angle θ between the electric current density $\boldsymbol{J}$ and the magnetic field $\boldsymbol{B}$, weighted by $|\boldsymbol{J}|$; and the $\langle |f_i| \rangle$ metric, the volume-averaged divergence of the magnetic field (see a more complete description in He et al. 2022). In addition, the total magnetic energy E_{tot} is also obtained.

For the 2015 June 22 event, we perform three extrapolation runs with different bottom BC inputs and grid structures. The associated descriptions of the bottom BC inputs are listed in Table 1. The extrapolation *Run 1* employs the nonuniform embedded magnetogram with a FOV of $204'' \times 204''$ ($149 \times 149 \, \text{Mm}^2$). The higher-resolution GST/NIRIS magnetogram with a FOV of $50'' \times 46''$ ($37 \times 34 \, \text{Mm}^2$) has been embedded into a larger SDO/HMI map with $1'' \, \text{pixel}^{-1}$ resolution. The inner core region is thus constructed with a volume size of $50'' \times 46'' \times 16''$ ($37 \times 34 \times 12 \, \text{Mm}^3$) and a grid size of $0\rlap{.}''125$ (91 km). Two additional runs are conducted for comparison. *Run 2* is carried out based on the uniform SDO/HMI vector magnetogram in a FOV of $204'' \times 204''$,

with a rebinned spatial resolution at $1'' \, \text{pixel}^{-1}$, which forms a core region with a height of $16''$ (12 Mm, the same physical height as for *Run 1*). *Run 3* employs the uniform higher-resolution vector magnetogram from GST/NIRIS in a smaller FOV of $50'' \times 46''$ with a pixel size of $0\rlap{.}''125$. The volume size of the core region for *Run 3* is $50'' \times 46'' \times 2''$ (16 pixels in height). The corresponding NLFFF quality metrics are calculated in a larger volume of $192'' \times 192'' \times 96''$ ($140 \times 140 \times 70 \, \text{Mm}^3$) for *Run 1* and *Run 2*, and in a smaller domain of $62\rlap{.}''5 \times 53\rlap{.}''75 \times 37\rlap{.}''5$ ($46 \times 39 \times 27 \, \text{Mm}^3$) for *Run 3* alone. In Figure 2 the residuals from three runs all decrease to a small magnitude of about 10^{-6} toward the end of the iteration. As for divergence-freeness, all three runs become stable after $\sim$20,000 steps. Figure 2(b) shows that the convergence of the current-weighted sine metric in *Run 1* is more complex than in the other runs. In a larger domain of $192'' \times 192''$, the *CWsin* value for *Run 1* continues to decrease, but it is relatively higher ($\sim$0.6, $\langle\theta\rangle \sim 37°$) than the result from *Run 2* within 40,000 steps. Considering the nonuniform BC we applied for *Run 1*, this high *CWsin* value in a large domain may be due to the difference between the part of the updated outer bottom boundary from the HMI magnetogram and the potential field solution based on the inner GST magnetogram in *Run 1*. Therefore, we also calculate the *CWsin* values in a smaller domain for *Run 1* with a size of $62\rlap{.}''5 \times 118\rlap{.}''75$ on the bottom
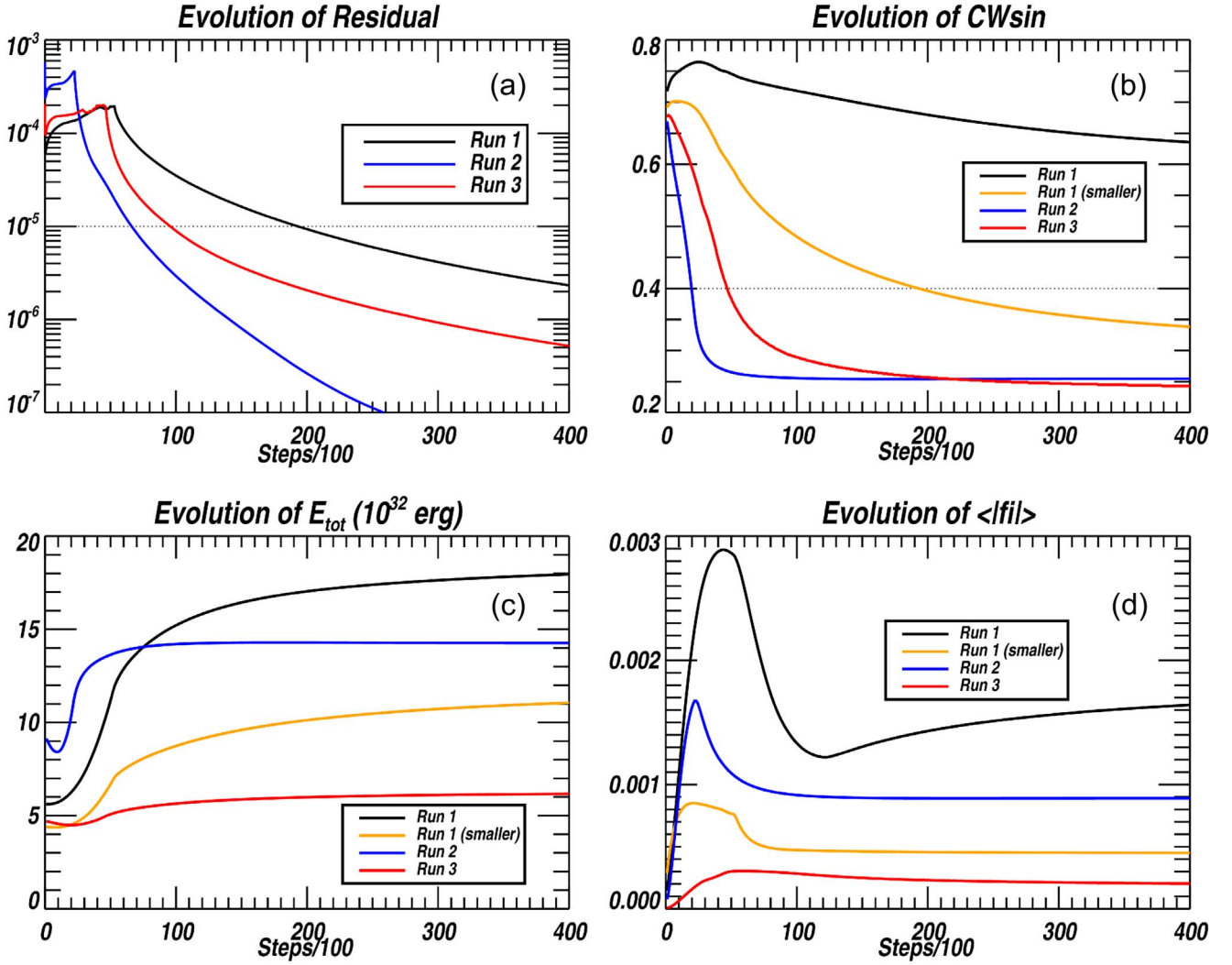
Figure 2. Evolution of the convergence metrics for the three extrapolation runs: (a) the residual of the magnetic field, (b) the current-weighted metric *CWsin*, (c) the total magnetic energy $E_{\rm tot}$, and (d) the divergence-freeness parameter $\langle |f_i| \rangle$. In practice, the metrics in (b)–(d) are calculated for different domains. The domains size for metrics calculation are $192'' \times 192'' \times 96''$ ($140 \times 140 \times 70$ Mm^3) for *Run 1* and *Run 2*, and $62''.5 \times 53''.75 \times 37''.5$ ($46 \times 39 \times 27$ Mm^3) for *Run 3*. Another smaller domain with a size of $62''.5 \times 118''.75 \times 37''.5$ ($46 \times 87 \times 27$ Mm^3), the same as the FOV of Figures 5 and 6, is additionally applied for *Run 1*.

Table 1
Boundary Conditions (BCs) for Different NLFFF Extrapolation Runs

Runs	Bottom BCs	Resolution	FOV of the Magnetogram	Count of Blocks	Computation Time (to 40,000 Steps)
Run 1	Nonuniform embedded magnetogram	Outer region: $1''$ Core region: $0''.125$	$204'' \times 204''$ (149×149 Mm^2)	41,040	157 hr
Run 2	Uniform SDO magnetogram at 17:36 UT	$1''$	$204'' \times 204''$ (149×149 Mm^2)	3080	12.5 hr
Run 3	Uniform GST magnetogram at 17:32 UT	$0''.125$	$50'' \times 46''$ (37×34 Mm^2)	13,850	52.5 hr

Note. All computations are performed with 19 cores on a 24-core local desktop with 48 GB memory and $1'' \sim 730$ km.

boundary (orange curves in Figure 2) as a consistency check, which reduces to ~ 0.34 ($\langle \theta \rangle \sim 20°$) after $\sim 40,000$ steps. This corresponds to the main part of the volume in which the subsequent topological analysis will be performed (see Section 4). For reference, the *CWsin* value for *Run 3* becomes almost stable and equal to *Run 2* after 25,000 steps. For the magnetic energy $E_{\rm tot}$ in a larger domain, *Run 2* becomes stable,

while *Run 1* shows a gradual increasing trend. For a smaller domain, the evolution of $E_{\rm tot}$ for *Run 3* and *Run 1* (smaller) becomes stable with a similar trend. $E_{\rm tot}$ is also higher than the corresponding potential field energy $E_{\rm pot}$ for all three runs. The computational time for three extrapolation runs varies and is generally proportional to the count of blocks, as shown in Table 1. To account for the low-lying magnetic structures for
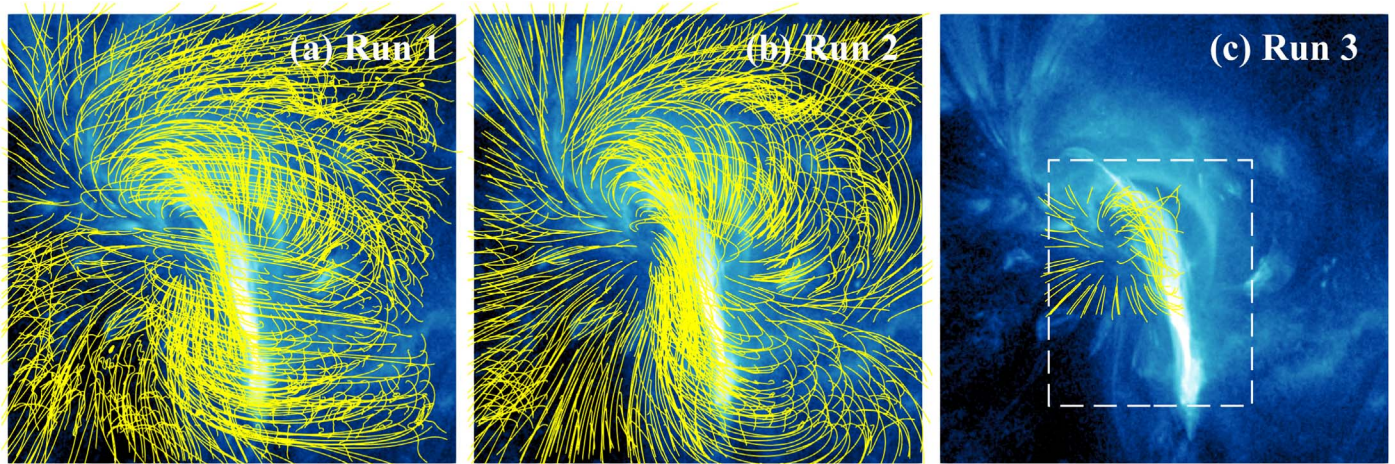
Figure 3. Magnetic field lines from three extrapolation runs within a height range of [0″, 60″] ([0, 44 Mm]) overplotted on the coaligned AIA 131 Å image at 17:36 UT. Panels (a) and (b) show field lines from *Run 1* and *Run 2* rooted in the same set of uniformly distributed seed points in a FOV of 190″ × 190″ (139 × 139 Mm²), which is similar to Figure 1(a). Panel (c) shows field lines from *Run 3* in a smaller FOV due to the limited computational domain of *Run 3*. The dashed white box indicates the FOV of Figure 7.

Table 2
NLFFF Quality Metrics for Force-freeness and Divergence-freeness

Runs	CWsin	$\langle |f_i| \rangle$	$E_{\nabla \times B}$	$E_{\nabla \cdot B}$
Run 1 (smaller)	0.338	4.50×10^{-4}	0.219	2.10×10^{-2}
Run 2	0.255	8.90×10^{-4}	0.161	3.76×10^{-2}
Run 3	0.243	2.02×10^{-4}	0.157	1.97×10^{-2}

Note. *Run 1* (smaller) shows the metrics calculated in a subvolume of *Run 1* with a domain size of $62\rlap{.}{''}5 \times 118\rlap{.}{''}75 \times 37\rlap{.}{''}5$ (46 × 87 × 27 Mm³). The corresponding quality metrics are calculated based on domain sizes of 192″ × 192″ × 96″ (140 × 140 × 70 Mm³) for *Run 2* and $62\rlap{.}{''}5 \times 53\rlap{.}{''}75 \times 37\rlap{.}{''}5$ (46 × 39 × 27 Mm³) for *Run 3*.

the nonuniform grid configurations and the available computational resources, the core regions with the same and modest physical heights are assigned for *Run 1* and *Run 2*. Significantly more blocks are therefore created in *Run 1* with a smaller grid size, which takes more time to converge. In general, the computational time can be shortened significantly with a smaller core region. For example, another run with a similar setting as *Run 1* for a core region at a height of 16 pixels (2″, 1.46 Mm) took about ∼19 hr to converge (40,000 steps) with the same computational resource.

To obtain a converged and consistent result for the later analysis, we further check the quality of these extrapolation results with additional quality metrics for force-freeness and divergence-freeness. Here we show the comparison of NLFFF quality metrics at 40,000 iteration steps from three extrapolation runs in Table 2. For *Run 1*, the additional metrics in a smaller volume ($62\rlap{.}{''}5 \times 118\rlap{.}{''}75 \times 37\rlap{.}{''}5$) are derived. Similarly, the additional metrics for *Run 2* and *Run 3* are also calculated, with volume sizes of 192″ × 192″ × 96″ and $62\rlap{.}{''}5 \times 53\rlap{.}{''}75 \times 37\rlap{.}{''}5$, respectively. The *CWsin* values for all three runs are around 0.24–0.34 ($\langle \theta \rangle \sim 14°$–20°), which are consistent with other NLFFF extrapolation results for realistic solar magnetograms (DeRosa et al. 2009; Jiang & Feng 2013). Given that the small-scale structures in the magnetograms with a weak magnetic field may increase the *CWsin* value due to weak currents, we also evaluate the force-freeness and divergence-freeness with two additional metrics, $E_{\nabla \times B}$ and

$E_{\nabla \cdot B}$, which estimate the residual force in the extrapolation results. The residual force comes from two parts: one part is the Lorentz force $(\nabla \times B) \times B$, and the other part is due to the nonvanishing divergence of the magnetic field $B \nabla \cdot B$ from the numerical errors (see the detailed descriptions in Duan et al. 2017). The results of the two additional metrics for all extrapolation runs are small, on the same orders of magnitude, and consistent with the previous reports (Jiang & Feng 2013; Duan et al. 2017; He et al. 2022). Thus, these extrapolation results extracted for the aforementioned smaller volume can be considered as converged solutions and are to be further analyzed and compared with observations.

As a routine and qualitative validation of the extrapolation results, Figure 3 shows a general comparison between an AIA 131 Å image and each extrapolation run with arbitrarily selected magnetic field lines rooted in the same set of seed points. In general, the distribution of field lines from *Run 1* is similar to that of *Run 2*, and both results match the large-scale coronal structures in the coaligned AIA 131 Å observation well, while the field lines in Figure 3(a) show a more compact shape near the flare core region than Figure 3(b). In contrast, Figure 3(c) exhibits a finer field line connectivity pattern around the center, which is confined in a smaller FOV given the limited computational domain of *Run 3*.

4. Results from Extrapolations and Observations

Before the main flare eruption, two small-scale precursor brightenings were identified as P1 and P2 near the PIL at ∼17:24 UT (P1) and ∼17:42 UT (P2) from the study using the high-resolution GST observations by Wang et al. (2017). Parts of the results from that analysis are reproduced in Figures 4(b)–(g). Figure 4(a) shows the GOES X-ray flux during the flare precursors. Two small peaks appear before the main flare eruption. These impulsive emission times of the GOES X-ray flux also coincide with the corresponding Hα brightenings as marked. Figures 4(b)–(g) are regenerated from Wang et al. (2017) to show the structural evolution of the flare precursors from the high-resolution GST/Hα observations. As shown in panels (b) and (d), the brightening P1b and P2a ("a" and "b" for each precursor period are named by Wang et al. (2017) based on the chronological order of their occurrence times) are almost
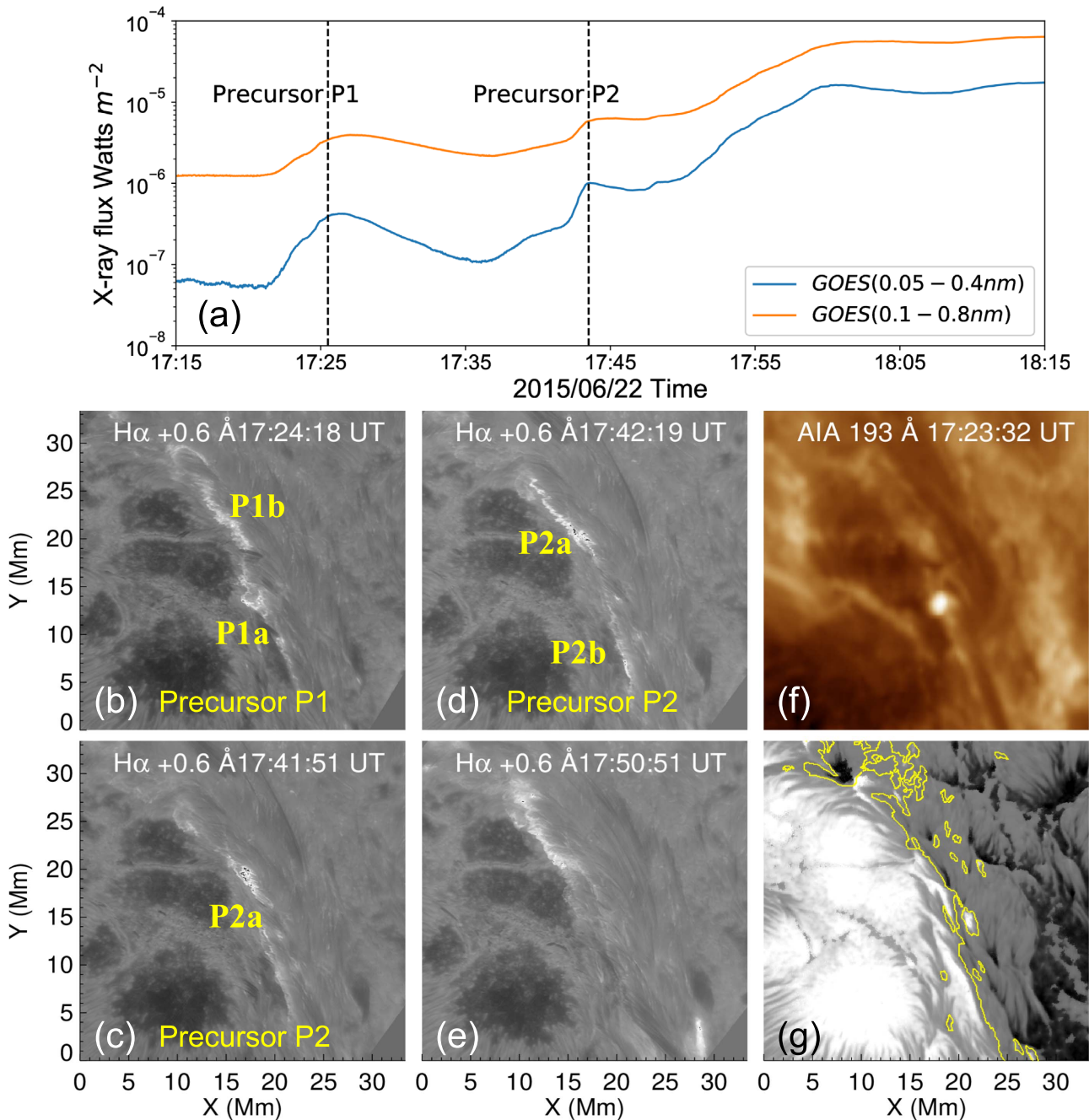
Figure 4. Precursor brightenings and associated observations. Panel (a) shows the GOES X-ray flux during the precursors. The two dashed lines mark the emission times for the two precursors that occurred at ~17:25 UT and ~17:43 UT. Panels (b)–(e): Structural evolution of the Hα brightenings P1a/P1b and P2a/P2b from the GST observations as identified by Wang et al. (2017) before the peak of the main flare (reproduced from Figure 1 in Wang et al. 2017). Panel (f): Corresponding image observed in the SDO/AIA 193 Å wavelength. Panel (g) shows the corresponding GST/NIRIS magnetogram of the B_z component. The yellow contour marks the PIL.

cospatial, while the P1a lies southward in a relatively different area from the brightening P2b. The corresponding GST/NIRIS magnetogram of the B_z component is presented in panel (g) and is overplotted with the PIL (shown by the yellow contour). During precursor P1, a brightening point was also observed in the coaligned SDO/AIA 193 Å image in panel (f), which is located close to the P1a brightening region.

4.1. Field Line Connectivity and GST Observations

To have a better understanding of the fine-scale structures in the 3D volume for the precursor brightenings, we compare the

available GST/Hα observations with the 3D coronal magnetic field topology from the static extrapolations *Run 1* to *Run 3*. Figure 5 illustrates the selected magnetic field line connectivity near precursor P1. First, two areas of interest for regions P1a and P1b are identified from the GST/Hα image at 17:24:18 UT in light blue scales (the same as Figure 4(b)) when the brightening intensity of a pixel is greater than a certain threshold in Figure 4(b). Two groups of such brightening pixels from P1a and P1b are selected and are shown in red (cyan) corresponding to the positive (negative) magnetic field polarity. The majority of the pixels are in red with a positive magnetic polarity, and the corresponding conjugate footpoints in cyan
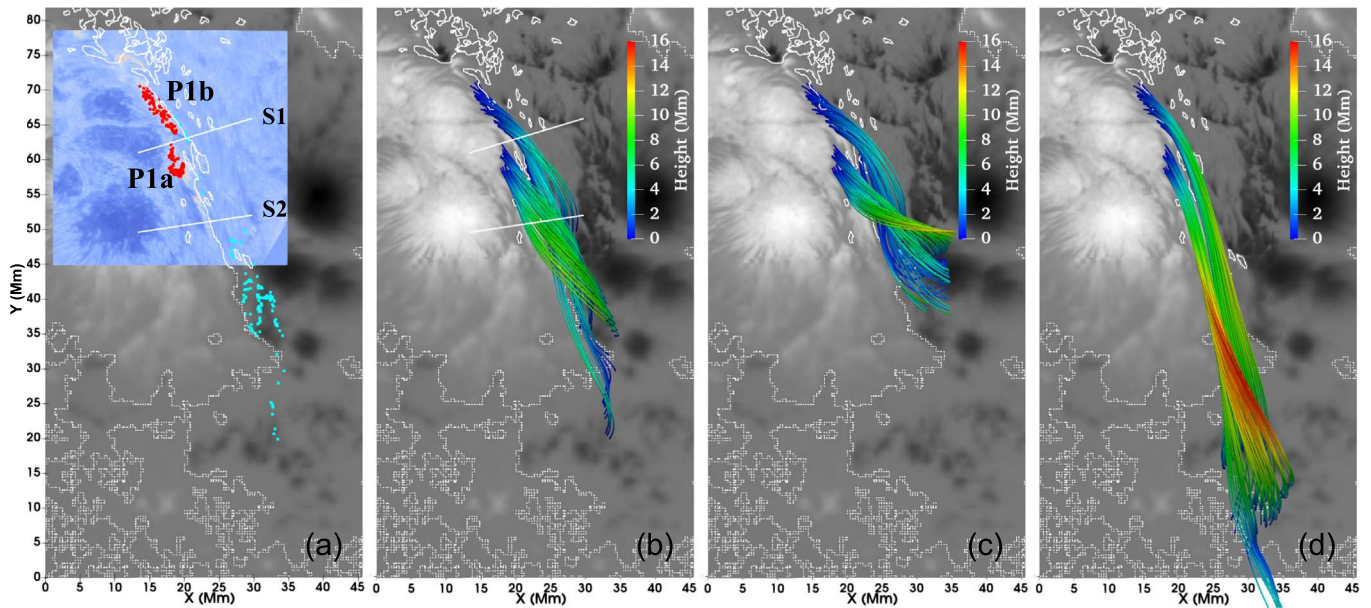
Figure 5. Analysis of selected magnetic field line connectivity near the precursor brightening P1. (a) Two groups of brightening pixels from P1a and P1b are selected over the GST/Hα+0.6 Å image (in light blue shades) at 17:24:18 UT together with their conjugate field line footpoints based on the extrapolation result from *Run 1*. They are color-coded by the magnetic polarity of the corresponding field line footpoints on the bottom boundary: positive in red, and negative in cyan. Panels (b)–(d) show the field lines that originate in the red points in panel (a) for all three NLFFF extrapolation runs (Runs 1, 3, and 2), which are colored by height. In each panel, the B_z map for *Run 1* on the bottom boundary is drawn in gray scales, and the PIL is indicated by the white contours. In panels (a) and (b), the two white lines S1 and S2 indicate the positions of two vertical slices that are displayed in Figures 9 and 10.

are marked across the PIL to the south based on the result from *Run 1*. Then the field lines that originate in the red points for all three NLFFF extrapolation runs are drawn for comparison and are colored by the vertical height along each field line in panels (b)–(d).

Most field lines from *Run 3* in Figure 5(c) are short-sheared arcades that appear within the FOV of the GST observation. The conjugate footpoints for the field lines originating in P1a are mainly attached to a major negative-polarity region of the background GST magnetogram, while the field lines from P1b are generally open and exit the limited computational domain. The field lines from *Run 2* are less sheared and extend farther than those from the other two runs. The long field lines in panel (d) come from P1a and P1b and extend to an area beyond the FOV of the GST magnetogram and farther southward of the cyan dots in panel (a). It is shown that some field lines from P1a in panel (d) are not closed within the selected domain, as shown. In contrast, the corresponding field lines from *Run 1* in panel (b) show conjugate negative-polarity footpoints (cyan dots in panel (a)) that extend beyond the FOV of the GST magnetogram, but are well within the FOV of the HMI magnetogram and across the main PIL between the two main positive and negative polarities. The group of selected field lines from P1b in panel (b) stays closed on the bottom boundary, while another group of field lines from P1a appears as a shorter sheared arcade and lies above the group that originates in P1b. We can see that the field line bundles in *Run 1* and *Run 3* reach a similar maximum height of ∼11 Mm (15″). From these comparisons, *Run 1* shows a reasonable consistency for the sheared arcade structures shown across the main PIL, where the two strong polarity regions are separated based on the GST and HMI magnetograms. The results for the other two runs are clearly affected by the sizes of their computational domains, with each maintaining a uniform grid setting.

For precursor P2, we also draw the field lines originating from chosen brightening pixels based on similar criteria for the GST/Hα observation at 17:42:19 UT, as presented in Figure 6. Similar to Figure 5, the field lines from *Run 1* in Figure 6(b) show magnetic structures corresponding to the precursor brightenings, with both a fine scale and a spatial extent along the main PIL confined within the strong field regions, albeit at lower heights. The Hα observations show that the brightening region P2a is nearly cospatial with P1b, whereas another region, P2b, lies in a different area from P1a. In terms of the height distribution, the field line bundle originating in P2b is situated at a lower height than the field lines from P1a, while the field lines from P1b and P2a have similar heights. As a general feature, the two groups of field lines from *Run 1* lie almost parallel to the PIL. Moreover, the positive-polarity footpoints of the sheared field line bundle from P2b are close to a part of the conjugate negative footpoints from P2a, as indicated by the red and cyan points in Figure 6(a), which configuration is potentially favorable for magnetic reconnection. Further topological analysis results are presented in Section 4.3.

4.2. Field Line Connectivity and AIA Observations

Due to the constraint of the limited FOV, a fine-scale GST observation is not available in a larger FOV encompassing the pairs of conjugate field line footpoints in the negative-polarity regions. To further verify the identified conjugate negative footpoints from the extrapolation *Run 1*, we also compare the field line connectivity with the corresponding *SDO*/AIA observations in a larger FOV (the white box marked in Figure 3(c)) to find its connection to the precursor brightenings. In Figure 7, a series of AIA observations during the precursor P1 are used as the background images along with the extrapolated field line bundles from *Run 1*. In panel (a), the
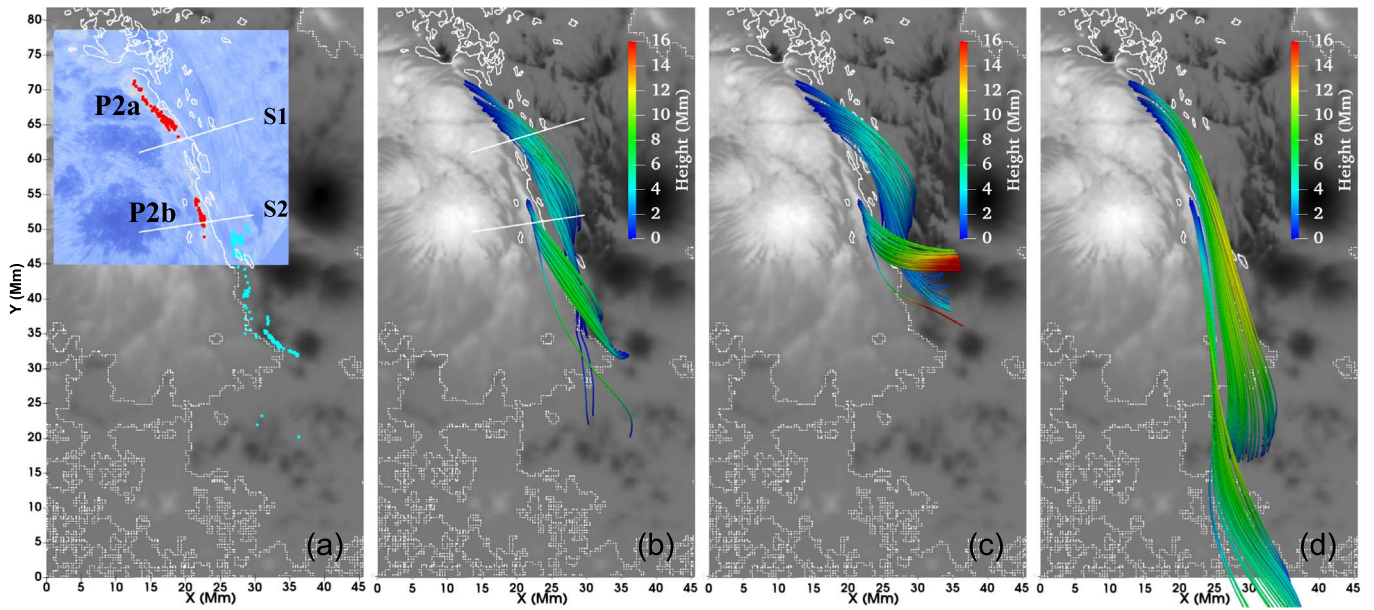
Figure 6. Similar analysis for the selected field lines corresponding to the precursor brightening P2, based on the GST/Hα+0.6 Å image at 17:42:19 UT and the extrapolation results from all three runs. The format is the same as in Figure 5.
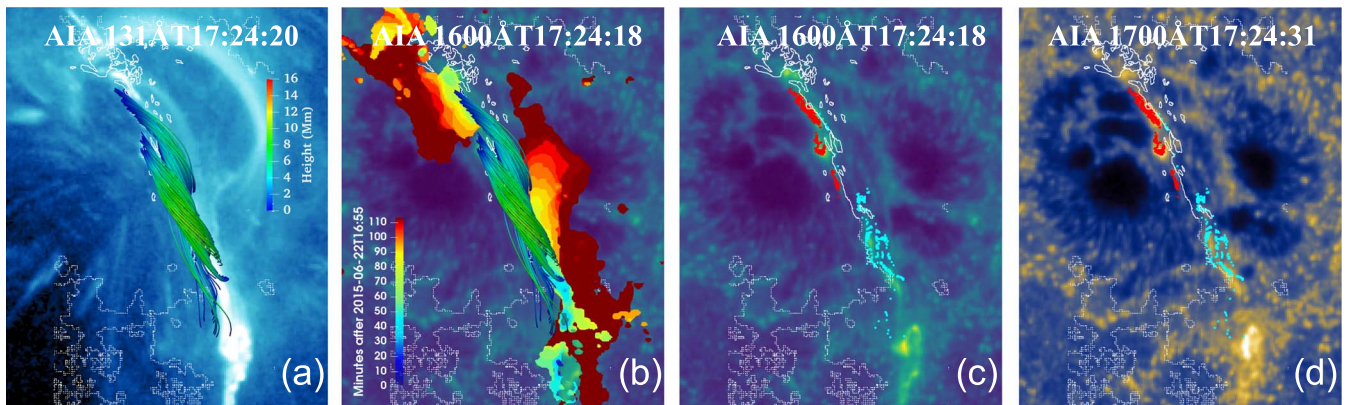

Figure 7. Comparison between the field line connectivity and AIA observations in different wavelengths. Panel (a) All selected field lines from *Run 1* in Figures 5 and 6 are superimposed on the AIA 131 Å observation. Panel (b) Contours of flare ribbons colored by the elapsed time since 16:55 UT (see the color bar) are overplotted with the set of field lines over an AIA 1600 Å image. Panels (c)–(d) The footpoints with positive (red) and negative (cyan) magnetic polarity for the set of field lines are drawn over the corresponding AIA 1600 and 1700 Å images.

field lines that originate in the selected Hα brightening pixels during precursors P1 and P2 are overplotted, and they agree well with the central hot loops in AIA 131 Å at 17:24 UT. In addition, in panel (b), the flare ribbon brightenings are also marked and color-coded by the elapsed time since 16:55 UT. The positive and negative footpoints of the identified field lines from precursors P1 and P2 are overlaid on AIA observations in panels (c)–(d). During precursor P1, the identified positive footpoints (red) from *Run 1* near P1a and P1b are cospatial with the brightening patches that are observed simultaneously in the AIA 1600 and 1700 Å wavelengths. The identified negative footpoints partially overlap with the brightening patches to the south in panels (c) and (d). Furthermore, as the flare ribbons can be used as an estimate for footpoints of reconnected magnetic field lines (Qiu et al. 2002, 2004), the overall flare ribbon evolution is superimposed in Figure 7(b). It indicates the initiation of the main flare reconnection closer to the PIL at earlier times and the subsequent extension of the ribbons away from the PIL when reconnection proceeds during the main

phase of the flare. Most footpoints of the multiple bundles of field lines identified from precursors P1 and P2 are located inside or near the flare ribbons at earlier times, which offers additional evidence in support of this magnetic field configuration for the precursor magnetic reconnection between low-lying arcades followed by the main phase flare reconnection (see, e.g., Moore et al. 2001).

4.3. Additional Topological Analysis near the Precursors

From the previous comparisons between the extrapolations and observations, several groups of sheared arcades over the main PIL have been successfully reconstructed as corresponding to the Hα precursor brightenings. The conjugate footpoints of precursor brightenings based on the extrapolation *Run 1* are also consistent with the alternative and subsequent brightening regions in the AIA observations. The questions remain, however, how the potential sites for magnetic reconnection can be found, how precursor brightenings evolve,
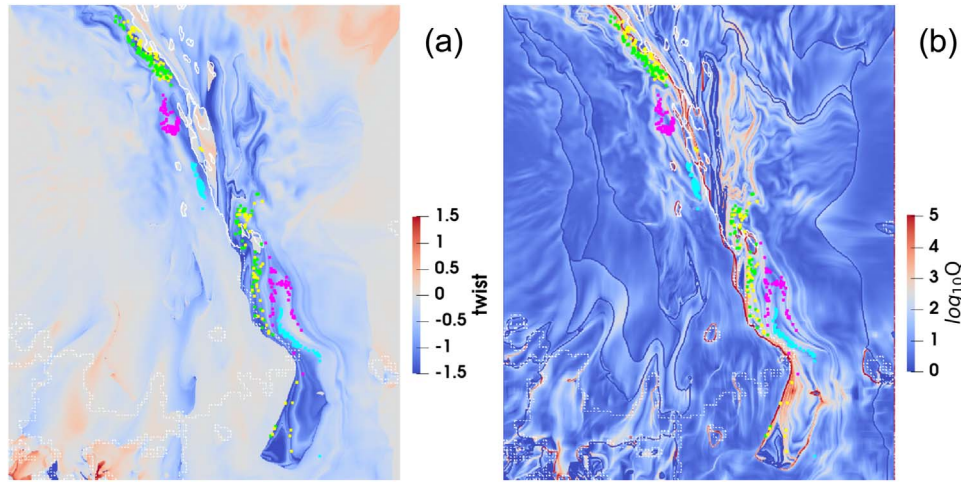
Figure 8. The top views of the distributions of (a) the twist number T_w and (b) the squashing degree Q (in base-10 logarithmic scale) on the bottom boundary. The footpoints for the four groups of field lines illustrated in Figures 5 and 6 are overlaid in different colors: precursor P1a in magenta, P1b in yellow, P2a in green, and P2b in cyan.
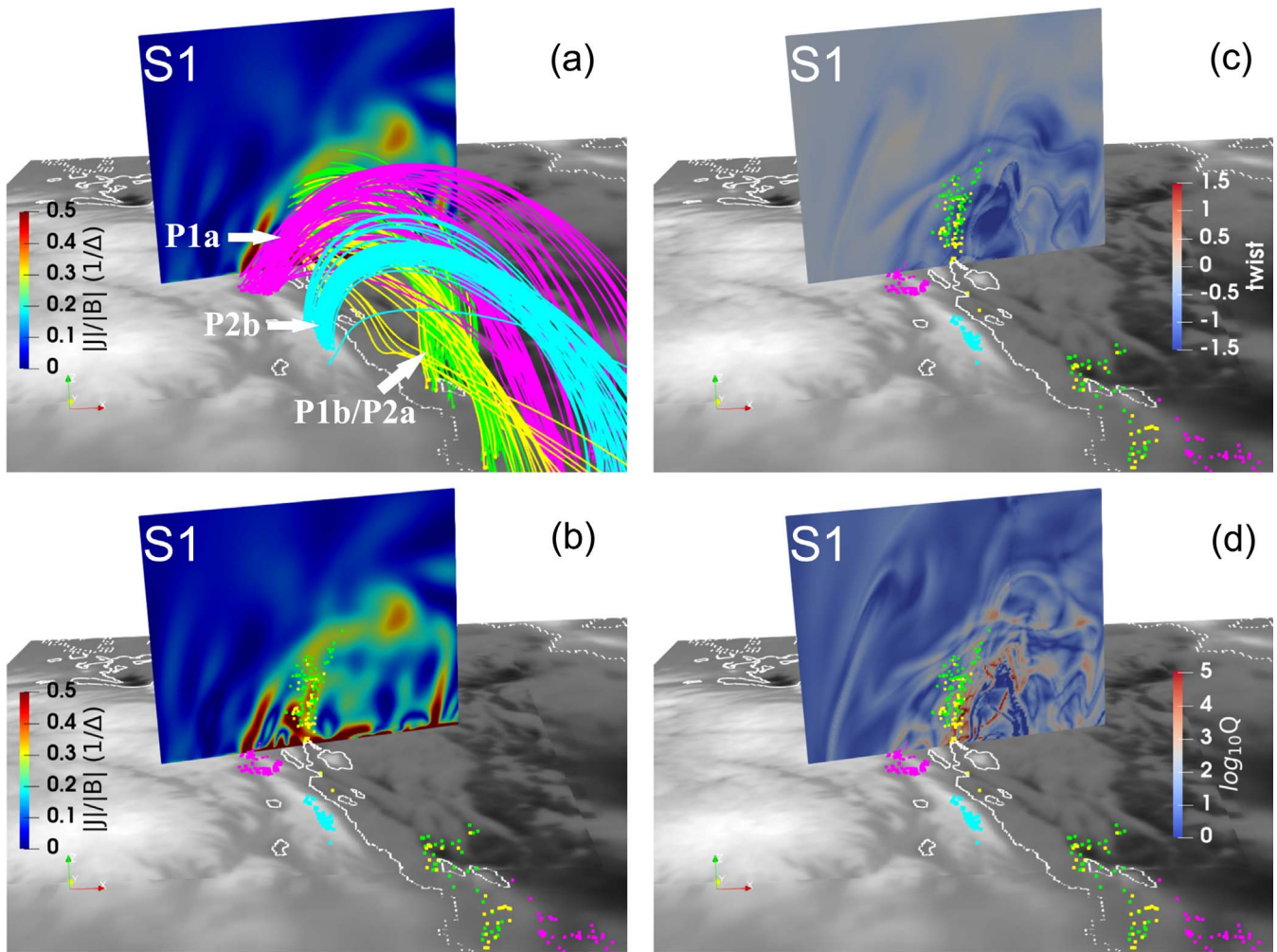

Figure 9. Topological analysis of the field lines corresponding to brightenings P1 and P2 near the vertical slice S1 (location marked in Figures 5 and 6). Panel (a) The distribution of $|\boldsymbol{J}|/|\boldsymbol{B}|$ in slice S1. The identified field lines corresponding to precursor P1a (magenta), P1b (yellow), P2a (green), and P2b (cyan) are also shown and marked. Panel (b) The same distribution on S1 as in panel (a), but with the corresponding magnetic field line intercepting points in the same colors as the field lines overplotted on the vertical slice S1 and the bottom layer. The intercepting points are also drawn in panels (c) and (d). Panels (c) and (d) show the distributions of the twist number T_w and the squashing degree Q in slice S1, as indicated by the color bars. For all panels, the B_z map with the PIL highlighted in white contours is drawn on the bottom layer.
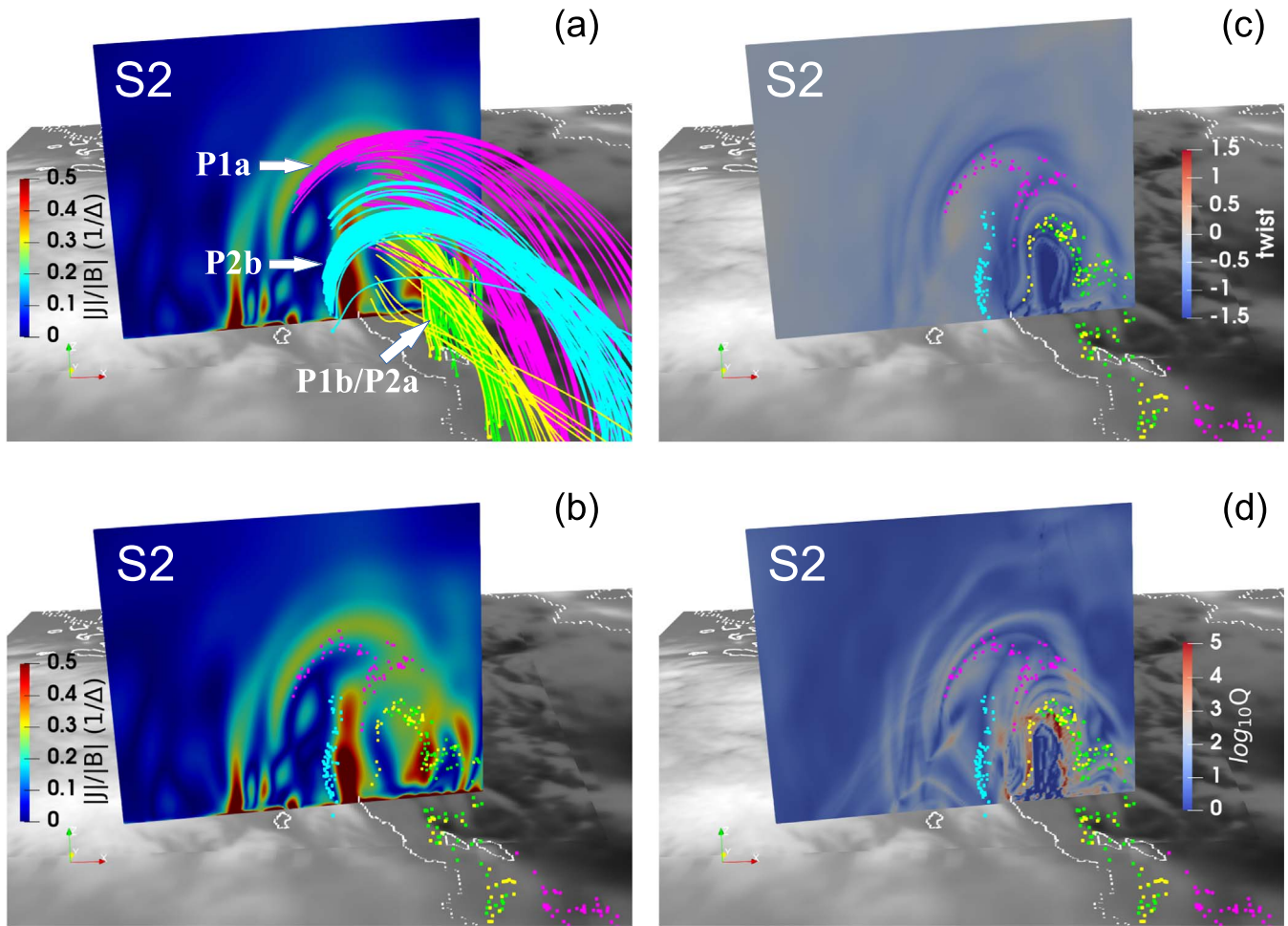
Figure 10. Similar analysis as shown in Figure 9, with the distributions of the corresponding topological parameters on the vertical slice S2. The format is the same as in Figure 9. The same sets of the magnetic field lines and the intersection points with corresponding colors are shown.

and how the subsequent reconnection sequence can be determined. To answer these questions, especially the first question, additional parameters such as the normalized current density (equivalent to $|J|/|B|$, in units of $1/\Delta$, where a uniform grid size Δ is used), the magnetic twist number T_w, and the squashing degree Q are calculated to analyze the magnetic topology in a specific volume. The magnetic twist number T_w gives a good estimate of how many turns two infinitesimally close field lines wind about each other (Berger & Prior 2006; Liu et al. 2016). The squashing degree Q quantifies the change of the magnetic connectivities (Demoulin et al. 1996; Titov et al. 2002). For example, complex 3D magnetic structures can be distinguished near high Q regions, where the gradient of the field line connectivity as measured by the Q value is large.

The top views of the twist number T_w and the squashing degree Q distributions on the bottom boundary are shown in Figure 8, along with the footpoints from the identified field lines corresponding to the precursor brightenings P1 and P2. They again show the spatial distribution of the field line footpoints for P1 and P2 along and within the extent of the main PIL, which is characterized by a sharp ridge-like feature in these parameter distributions. Figures 9 and 10 show the distributions of $|J|/|B|$, the twist number T_w, and the squashing degree Q in the two vertical slices, S1 and S2, as marked in Figures 5 and 6. The extrapolation result based on *Run 1* is obtained with the embedded vector magnetograms at 17:32 UT

(GST) and 17:36 UT (HMI), which provides a snapshot of the magnetic field topology at a time between precursors P1 and P2. For the slice S1 in Figure 9, the field lines from P1b and P2a (shown in yellow and green, respectively) go through a region with a relatively high current density. In addition, the squashing degree Q around these field lines exhibits a complex pattern that is intermixed with high values. This complexity also remains around the intercepting field line points in slice S2 in Figure 10(d), indicating the potential sites for magnetic reconnection between these field lines, which could result in the cospatial brightenings at their footpoints, as observed in areas P1b and P2a. Considering the magnetic topology near other brightenings (P1a and P2b), the field line bundles originating from P1a and P2b (pink and cyan) are next to the other two, with modest Q values in Figure 10(d). The twist numbers are all insignificant for these field lines. However, from the distribution of the intercepting points of different field lines in slice S2 in Figure 10(b), the cyan field line bundle from P2b is lower than the pink bundle from P1a, and it is close to the yellow/green field line bundles from P1b/P2a. In addition, the cyan field lines from P2b and the green field lines from P2a are separated by a high $|J|/|B|$ region in Figure 10(b). This configuration may correspond to the initial stage of the tether-cutting reconnection scenario described in van Ballegooijen & Martens (1989) and Moore et al. (2001). That is, the magnetic reconnection among and between the sheared magnetic flux

bundles as shown across the main PIL may take place, resulting in the brightenings of the associated field line footpoints without significant changes in their positions. This could be one result that might explain why the spatial features are consistent with the observed brightenings, but not the temporal changes. The purpose of this extrapolation is to provide a snapshot at a specific time. To examine the temporal change in the magnetic field topology is beyond its capability. Nonetheless, we also performed an additional extrapolation run for the embedded magnetogram around 17:48 UT, at a time that is a few minutes after P2. The result shows a similar magnetic field line topology for the precursor regions as we have presented in this section. This probably implies that the reconnection associated with the precursors only involved small amounts of flux, and the reconnection did not significantly change the flux distributions of the precursor regions. The small amount of flux change that is distributed outside the FOV of GST may not be captured by the SDO/HMI magnetogram with its modest spatial resolution.

5. Summary and Conclusions

In this study, we have applied the CESE-MHD-NLFFF extrapolation method to a nonuniform embedded magnetogram for the first time to study the fine-scale structures of precursors before the eruption of the main flare. Three extrapolation results are obtained with different bottom BCs and grid structures: *Run 1* with a nonuniform embedded magnetogram, *Run 2* with a uniform SDO/HMI magnetogram, and *Run 3* with a uniform GST/NIRIS magnetogram. In the convergence study, the residual and the divergence-freeness parameters for all three runs become sufficiently small during the iteration, while the force-freeness parameter shows a more complicated behavior. The *CWsin* value in a larger computational domain for *Run 1* is higher than the other results, but it is reduced to ~0.34 ($\langle\theta\rangle \sim 20°$) for a smaller volume in which the magnetic field topology is examined in detail. The deviation from a strictly force-free state in *Run 1* could be due to the nonuniform BC and grid structure, which were designed for the embedded magnetogram. Nonetheless, the *CWsin* values calculated in the regions of interest for all three runs after ~40,000 iteration steps are around 0.24–0.34 ($\langle\theta\rangle \sim 14°$–$20°$), which is consistent with prior NLFFF extrapolation results that are considered to be converged solutions for realistic solar magnetograms. After the converged results are obtained, we examined the reconstructed 3D magnetic field topology around the precursor brightenings and compared the field line connectivity with the GST/Hα and SDO/AIA observations. Additional topological features for the extrapolation *Run 1* are investigated by focusing on the fine-scale structures around the precursor brightenings and across the main PIL. The main results are listed as follows:

1. For all three extrapolation runs, the field line connectivity around the precursor brightenings is compared with the GST/Hα observations. The magnetic field lines originating from the precursor brightening regions based on *Run 1* exhibit a configuration of the fine-scale magnetic structures beyond the small FOV of GST, but are confined within the larger FOV of HMI, more consistent with the spatial extent of the main PIL between two main magnetic polarities. Multiple sheared flux bundles are found to overlie across the main PIL, with groups of footpoints rooted in the positive magnetic polarity regions and coinciding with each set of the observed Hα brightening patches, P1 and P2.

2. The selected field line bundles originating in the Hα brightening patches from *Run 1* show an overall shape that is consistent with the corresponding AIA observations in different wavelengths. The selected field lines agree well with the hot loops observed in the AIA 131 Å passband. Their footpoints are attached to the inner sides of the flare ribbons with the closest distances from the PIL, which indicates a potential configuration for the magnetic reconnection during the flare precursors at earlier times.

3. With the magnetic field topological analysis near the precursor brightenings based on the extrapolation *Run 1*, including the distributions of the normalized current density $|\boldsymbol{J}|/|\boldsymbol{B}|$, the magnetic twist number T_w, and the squashing degree Q, a plausible configuration for magnetic reconnection is found. These structures may correspond to the initial stage of the tether-cutting reconnection scenario, before the onset of the main flare, for instance.

These results based on *Run 1* represent the application of the CESE-MHD-NLFFF extrapolation method for an embedded photospheric magnetogram from the GST/NIRIS and SDO/HMI observations. By using different analyzing tools for the extrapolation results, together with additional observations, the fine-scale magnetic structures around flare precursors are found to be consistent with the associated high-resolution GST/Hα observations. We conclude that the reconstructed magnetic field line topology/connectivity across the main PIL from *Run 1* is more plausible for the subsequent magnetic reconnection among the sheared flux bundles, resulting in the corresponding precursor brightenings. We thus provide a viable approach to investigate the fine-scale structures associated with solar eruptions by combining the high-resolution magnetogram in a smaller FOV with another set of magnetogram in a larger FOV. By resolving the potential site for the small-scale precursors before the onset of the main flare eruption, this study demonstrates the merit of employing the ultrahigh-resolution magnetogram with its native resolution. The reconstructed magnetic field over the whole computation volume could also be further analyzed, and the results could contribute to improving our understanding on how to connect the small-scale energy-release processes and the main phase of solar eruptions at larger scales, including filaments, flares, and CMEs. This will be pursued in future studies.

ORCID iDs

Wen He ⦿ https://orcid.org/0000-0001-8749-1022
Ju Jing ⦿ https://orcid.org/0000-0002-8179-3625
Haimin Wang ⦿ https://orcid.org/0000-0002-5233-565X
Sushree S. Nayak ⦿ https://orcid.org/0000-0002-4241-627X
Avijeet Prasad ⦿ https://orcid.org/0000-0003-0819-464X

References

Awasthi, A. K., Jain, R., Gadhiya, P. D., et al. 2014, MNRAS, 437, 2249
Awasthi, A. K., Liu, R., Wang, H., Wang, Y., & Shen, C. 2018, ApJ, 857, 124
Bamba, Y., Kusano, K., Imada, S., & Iida, Y. 2014, PASJ, 66, S16
Bamba, Y., Lee, K.-S., Imada, S., & Kusano, K. 2017, ApJ, 840, 116
Benz, A. O. 2017, LRSP, 14, 2
Berger, M. A., & Prior, C. 2006, JPhA, 39, 8321
Bobra, M. G., Sun, X., Hoeksema, J. T., et al. 2014, SoPh, 289, 3549
Bumba, V., & Křivský, L. 1959, BAICz, 10, 221
Cao, W., Goode, P. R., Ahn, K., et al. 2012, in ASP Conf. Ser. 463, Second ATST-EAST Meeting: Magnetic Fields from the Photosphere to the Corona, ed. T. R. Rimmele et al. (San Francisco, CA: ASP), 291
Cao, W., Gorceix, N., Coulter, R., et al. 2010, AN, 331, 636
Carmichael, H. 1964, The Physics of Solar Flares, Proc. of the AAS-NASA Symp. on the Physics of Solar Flares, Vol. 50 (Washington, DC: NASA), 451
Chifor, C., Tripathi, D., Mason, H. E., & Dennis, B. R. 2007, A&A, 472, 967
Chiu, Y. T., & Hilton, H. H. 1977, ApJ, 212, 873
Demoulin, P., Henoux, J. C., Priest, E. R., & Mandrini, C. H. 1996, A&A, 308, 643
DeRosa, M. L., Schrijver, C. J., Barnes, G., et al. 2009, ApJ, 696, 1780
DeRosa, M. L., Wheatland, M. S., Leka, K. D., et al. 2015, ApJ, 811, 107

Duan, A., Jiang, C., He, W., et al. 2019, ApJ, 884, 73
Duan, A., Jiang, C., Hu, Q., et al. 2017, ApJ, 842, 119
Gary, G. A. 2001, SoPh, 203, 71
Gyenge, N., Ballai, I., & Baranyi, T. 2016, MNRAS, 459, 3532
He, W., Hu, Q., Jiang, C., Qiu, J., & Prasad, A. 2022, ApJ, 934, 103
Hirayama, T. 1974, SoPh, 34, 323
Hu, Q., Zhu, C., He, W., et al. 2022, ApJ, 934, 50
Jiang, C., & Feng, X. 2012, ApJ, 749, 135
Jiang, C., & Feng, X. 2013, ApJ, 769, 144
Jiang, C., & Feng, X. 2014, SoPh, 289, 63
Jiang, C., Feng, X., Fan, Y., & Xiang, C. 2011, ApJ, 727, 101
Jiang, C., Feng, X., Guo, Y., & Hu, Q. 2022, Innov, 3, 100236
Jing, J., Liu, N., Lee, J., et al. 2023, ApJ, 952, 40
Jing, J., Liu, R., Cheung, M. C. M., et al. 2017, ApJL, 842, L18
Jing, J., Xu, Y., Cao, W., et al. 2016, NatSR, 6, 24319
Kang, J., Inoue, S., Kusano, K., Park, S.-H., & Moon, Y.-J. 2019, ApJ, 887, 263
Kopp, R. A., & Pneuman, G. W. 1976, SoPh, 50, 85
Lemen, J. R., Title, A. M., Akin, D. J., et al. 2012, SoPh, 275, 17
Liu, C., Cao, W., Chae, J., et al. 2018, ApJ, 869, 21
Liu, N., Jing, J., Xu, Y., & Wang, H. 2022a, ApJ, 930, 154
Liu, R., Kliem, B., Titov, V. S., et al. 2016, ApJ, 818, 148
Liu, Y., Su, Y., Liu, R., et al. 2022b, ApJ, 941, 83
MacNeice, P., Olson, K. M., Mobarry, C., de Fainchtein, R., & Packer, C. 2000, CoPhC, 126, 330
Metcalf, T. R., De Rosa, M. L., Schrijver, C. J., et al. 2008, SoPh, 247, 269
Moore, R. L., Sterling, A. C., Hudson, H. S., & Lemen, J. R. 2001, ApJ, 552, 833
Qiu, J., Lee, J., Gary, D. E., & Wang, H. 2002, ApJ, 565, 1335
Qiu, J., Wang, H., Cheng, C. Z., & Gary, D. E. 2004, ApJ, 604, 900
Schou, J., Scherrer, P. H., Bush, R. I., et al. 2012, SoPh, 275, 229
Schrijver, C. J., De Rosa, M. L., Metcalf, T. R., et al. 2006, SoPh, 235, 161
Sturrock, P. A. 1966, Natur, 211, 695
Tappin, S. J. 1991, A&AS, 87, 277
Thalmann, J. K., Tiwari, S. K., & Wiegelmann, T. 2013, ApJ, 769, 59
Titov, V. S., Hornig, G., & Démoulin, P. 2002, JGRA, 107, 1164
van Ballegooijen, A. A., & Martens, P. C. H. 1989, ApJ, 343, 971
Wang, H., Liu, C., Ahn, K., et al. 2017, NatAs, 1, 0085
Wiegelmann, T., Inhester, B., & Sakurai, T. 2006, SoPh, 233, 215
Wiegelmann, T., & Sakurai, T. 2021, LRSP, 18, 1
Xu, Y., Cao, W., Ahn, K., et al. 2018, NatCo, 9, 46
Zhao, J., Su, J., Yang, X., et al. 2022, ApJ, 932, 95